Geophysical Journal International

Geophys. J. Int. (2014) **197,** 1705–1718
Advance Access publication 2014 April 29

doi: 10.1093/gji/ggu074

Off-fault damage and acoustic emission distributions during the evolution of structurally complex faults over series of stick-slip events

T. H. W. Goebel,[1,*] T. W. Becker,[1] C. G. Sammis,[1] G. Dresen[2] and D. Schorlemmer[2]

[1] *University of Southern California, Los Angeles, CA, USA. E-mail: thw.goebel@gmail.com*
[2] *German Research Centre for Geosciences, Potsdam, Germany*

Accepted 2014 February 24. Received 2014 February 19; in original form 2013 October 5

SUMMARY

Variations in fault structure, for example, surface roughness and deformation zone width, influence the location and dynamics of large earthquakes as well as the distribution of small seismic events. In nature, changes in fault roughness and seismicity characteristics can rarely be studied simultaneously, so that little is known about their interaction and evolution. Here, we investigate the connection between fault structure and near-fault distributions of seismic events over series of stick-slip cycles in the laboratory. We conducted a set of experiments on rough faults that developed from incipient fracture surfaces. We monitored stress and seismic activity which occurred in the form of acoustic emissions (AEs). We determined AE density distributions as a function of fault normal distance based on high-accuracy hypocentre locations during subsequent interslip periods. The characteristics of these distributions were closely connected to different structural units of the faults, that is, the fault core, off-fault and background damage zone. The core deformation zone was characterized by consistently high seismic activity, whereas the off-fault damage zone displayed a power-law decay of seismic activity with increasing distance from the fault core. The exponents of the power-law-distributed off-fault activity increased with successive stick-slip events so that later interslip periods showed a more rapid spatial decay of seismic activity from the fault. The increase in exponents was strongest during the first one to three interslip periods and reached approximately constant values thereafter. The relatively rapid spatial decay of AE events during later interslip periods is likely an expression of decreasing fault zone complexity and roughness. Our results indicate a close relationship between fault structure, stress and seismic off-fault activity. A more extensive mapping of seismic off-fault activity-decay has the potential to significantly advance the understanding of fault zone properties including variations in fault roughness and stress.

Key words: Microstructures; Seismicity and tectonics; Statistical seismology; Rheology and friction of fault zones; Dynamics and mechanics of faulting; Fractures and faults.

1 INTRODUCTION

The complexity of strain accumulation along tectonic plate boundaries, which are comprised of systems of faults, poses a challenge for the predictability of earthquakes. Earthquake rupture initiation and propagation is strongly influenced by the frictional properties and structure of faults. Faults are zones of high strain within the upper crust, consisting of a fault core surrounded by a zone of distributed damage (e.g. Caine *et al.* 1996; Ben-Zion & Sammis 2003). This damage zone consists of joints, cracks, pulverized rock and subsidiary faults over a wide range of length scales, and the embedded fault core contains a gouge layer, as well as anastomosing principal and secondary zones of slip localization (e.g. Chester & Logan 1986; Chester *et al.* 1993; Faulkner *et al.* 2003; Dor *et al.* 2006; Wibberley *et al.* 2008; Faulkner *et al.* 2010). The structure of fault zones varies along fault-strike and depends on both protolith composition and rock-fluid interactions (e.g. Schulz & Evans 2000; Faulkner *et al.* 2003, 2008; Smith *et al.* 2013). Current models of fault zone structure suggest that faults are heterogeneous but become less complex with increasing displacements so that most of the slip on mature faults occurs within zones of highly localized strain (e.g. Chester *et al.* 1993; Chester & Chester 1998; Ben-Zion & Sammis 2003). This is supported by geological observations of large off-set fault zones in Southern California (e.g. Chester & Chester 1998; Rockwell & Ben-Zion 2007). Fault evolution has additionally been

*Now at: Caltech Seismological Laboratory, Pasadena, CA, USA.

documented by decreasing numbers of fault stepovers (e.g. Wesnousky 1988), and decreasing geometric disorder of fault surface traces (Wechsler *et al.* 2010) with increasing cumulative displacements. These studies generally indicate a continuous evolution towards less complexity even after large amounts of slip (1–300 km) have been accumulated. This is in agreement with results from seismicity inferred fault smoothing which appears to be active at displacements of up to ∼300 km (Powers & Jordan 2010). However, other studies which examined roughness of exhumed fault surfaces suggested that large off-set faults remain in a state of constant complexity (Sagy *et al.* 2007; Candela *et al.* 2012), possibly due to decreasing rates of abrasional smoothing caused by gouge lubrication (Brodsky *et al.* 2011) or rupture related fault re-roughening (Bhat *et al.* 2004; Klinger 2010). The apparent discrepancies in studies on fault roughness reduction as function of fault maturity raise questions about the uniformity of fault evolution. Fault roughness reduction may be scale-dependent, or a transient process that is only active on relatively young faults.

A better documentation of fault evolution is vital for the understanding of many upper crustal processes. A reduction in fault roughness, for example, influences the characteristics of strain release during fault slip including slip distributions, stress drops and off-fault stresses (Power & Tullis 1995; Dieterich & Smith 2009; Candela *et al.* 2011a,b; Dunham *et al.* 2011). Moreover, the degree of slip localization and roughness reduction of evolving fault zones govern many fault processes related to fault-hydrology, fault-zone growth, earthquake-rupture dynamics and the near-fault distribution of seismic events (e.g. Ben-Zion & Sammis 2003; Wibberley *et al.* 2008; Faulkner *et al.* 2010; Powers & Jordan 2010). Similarly, the geometry of systems of faults controls local earthquake interactions and seismicity clustering. Models that include these fault-system-induced interactions can produce seismicity characteristics similar to regional observations and replicate observed statistical relations of natural seismicity, including aftershock clustering (e.g. Ward 2000; Rundle *et al.* 2004; Dieterich & Richards-Dinger 2010). Thus, a more detailed understanding of fault evolution and its controls on seismic event distribution is essential, not least for seismic hazard assessment.

Geologic observations of fault-zone structure are commonly limited to inactive, exhumed fault branches, so that an investigation of fault structure, fault evolution and associated variations in seismicity distributions is not straightforward. To overcome these limitations, we study fault evolution and seismic event distributions on complex fault zones in laboratory experiments under upper crustal stress-conditions. We present results from series of stick-slip experiments on laboratory-created fault zones during which we document stress, strain, and seismic activity as well as post-experimental fault structures. We previously tested the connection between roughness and seismicity-density distributions on planar surfaces with predefined roughness showing that the off-fault activity can be described by a power law which is controlled by fault roughness and normal stress (Goebel *et al.* 2014). The observed power-law distributions are in agreement with a theoretical study on the effects of fractal roughness on off-fault seismicity distributions (Dieterich & Smith 2009). We extend the previous experiments through the creation of series of stick-slip events on structurally complex fault zones that developed from incipient, natural fracture surfaces. The current study is divided into three parts: Initially, we compare fault zone structure observed in computer tomography (CT) scans, photographic images and thin sections with acoustic emission (AE) density distributions. We then investigate changes in AE density distributions with successive stick-slip events as possible indicator for progressive fault smoothing. Finally, we examine the connection between variations in normal stress and seismic off-fault activity distributions.

Table 1. Mechanical data and loading conditions of the four presented experiments. The length of the saw-cut notches increased from WG04 to WG08 which led to a reduction of the length of the rough surface area. Initially, samples were fractured at $P_c = 75$ MPa and then reloaded at 150 MPa. l_{RS}: approximate length of the rough fracture surface, σ_{diff}: maximal differential stress during sliding, U_z: maximum vertical displacement of loading piston, σ_n: normal stress, and τ: shear stress. σ_n and τ were corrected for notch length and change in fault area due to slip (see text for details).

Experiment	l_{RS} (cm)	σ_{diff} (MPa)	U_z (mm)	σ_n (MPa)	τ (MPa)
WG04	5.0 ± 0.15	365 ± 6	3.0 ± 0.003	261 ± 6	198 ± 6
WG05	4.2 ± 0.15	296 ± 6	4.1 ± 0.003	372 ± 6	276 ± 6
WG07	3.7 ± 0.15	293 ± 6	4.3 ± 0.003	237 ± 6	170 ± 6
WG08	3.0 ± 0.15	288 ± 6	3.7 ± 0.003	280 ± 6	224 ± 6

2 DATA AND METHOD

We show results from four frictional sliding experiments (WG04, WG05, WG07 and WG08) on Westerly granite surfaces, loaded under triaxial compression. Prior to loading, the rock samples were prepared with saw-cut notches at 30° angles to the loading axis to concentrate deformation towards the centre of the samples (see Fig. S1 and Goebel *et al.* 2012, for schematic representations of sample geometry and loading conditions). Initially, we fractured the intact part between the notches. We then increased the confining pressure to lock the faults and loaded the samples axially resulting in series of stick-slip events (see supporting information for more details). The current study focuses on results from the stick-slip sliding phase of these experiments. This phase was generally conducted at a constant axial displacement rate (20 µm min^{-1}, and corresponding axial strain rate: $\dot{\epsilon} \approx 3 \times 10^{-6}$ s^{-1}) and constant confining pressure ($P_c = 150$ MPa). Changes in differential stress were determined from force measurements of an external load cell. Fault normal stresses were computed under consideration of changing fault geometries, that is, we corrected for different notch depths and changes in effective fault surface area due to slip (Scott *et al.* 1994; Tembe *et al.* 2010). A summary of loading conditions, sample geometry, and stresses can be found in Table 1.

The deformation along the laboratory-created fault zones was connected to high AE activity. To document the AE activity, we employed a high-speed (10 MHz sampling frequency) and high-accuracy (16 bits amplitude resolution) data acquisition system (see Stanchits *et al.* 2006, for details). AE events were recorded using a miniature seismic-array, consisting of 16 piezo-electric transducers. AE event locations were determined from traveltime inversions of automatically picked first arrival times. The location-uncertainty of AE hypocentres was estimated at 1–4 mm, depending on the proximity of an event to the limits of seismic array coverage. The total number of located AEs varied between ∼30 000 to ∼100 000 for the different experiments (see Goebel *et al.* 2013a).

The analysis of fault-normal AE distributions within this study largely follows Goebel *et al.* (2014). Initially, we projected the recorded AE hypocentre locations into the corresponding, best-fitting fault coordinate systems. The spatial decay of AE events relative to the fault was determined from linear density estimates (e.g. Silverman 1986) analogous to previous studies of natural seismicity (Hauksson 2010; Powers & Jordan 2010). Fault-normal AE densities were computed by sampling a constant number (N) of

nearest-neighbour events starting from the fault centre (Silverman 1986). We determined the density of the individual samples, which is proportional to the fault-normal distance of the *N*th event. The density was then normalized by the total fault area and experiment duration. Changes in the sample size, *N*, mainly influence the data scatter, and the characteristics within the distribution tail, whereas the slopes remained stable (see Fig. S2). Prior to AE density estimates, we stacked the AE activity from both sides of the faults and test for symmetry of AE event distributions relative to the fault axis. The symmetry test involves comparing the cumulative fault-normal-distances from each side of the fault and computing the maximum Kolmogorov–Smirnov (KS) distances for a set of possible fault centre locations. The 'true' fault axis minimizes the KS-distance between both fault sides. Details about the estimation of AE density distributions and sensitivity to fault orientation and centreing can be found in the supporting information.

The fall-off in AE density distributions could be described by a power law. The power-law exponents were determined using a maximum likelihood estimate (e.g. Newman 2005; Clauset *et al.* 2009). The corresponding minimum bounds were computed through maximizing the fit between observed and modelled, power-law-distributed data. The best-fitting power-law parameters minimize the KS distances between the observed and the modelled cumulative distributions (Clauset *et al.* 2009). We tested the statistical significance of the power-law fits by bootstrap resampling. To this aim, we created 10 000 synthetic data sets based on the estimated power-law parameters and compute the goodness-of-fit between synthetic data and the model as well as empirical data and the model. The resampling method evaluates how much of the difference between the model and the data can be explained by random, statistical variations as opposed to systematic variations, for example, due to applying an incorrect model. Following Clauset *et al.* (2009), we chose a significance level of 0.1 as sufficient to establish the power-law hypothesis. We tested the influence of hypocentral uncertainties on power-law distributions using synthetic data (Goebel *et al.* 2014). Close to the fault, the convolution of power-law and Gaussian uncertainties is controlled by location uncertainties whereas at larger distance the power law dominates the distributions. The more distant portion of the distribution can be used to estimate the power-law parameters and the influence of the Gaussian can be removed by a simple linear correction using the expected uncertainty, if both uncertainty and power-law exponent are not very large. The synthetic tests also revealed that the minimum power-law bound can lie slightly beneath the hypocentral uncertainties. A more detailed description of the here employed tests for power-law behaviour and corresponding parameter estimates can be found in Goebel *et al.* (2014).

3 RESULTS

Stick-slip type fault motion is characterized by increasing stresses during interslip periods and an abrupt decrease during failure, which can be considered a laboratory analogue to natural earthquake behaviour (e.g. Brace & Byerlee 1966). We strove to mimic the natural faulting process through creating series of stick-slip events on structurally complex fault zones allowing for abrupt earthquake-like stress release and fault evolution over several seismic cycles. As a consequence, the differential–stress curves during our experiments were generally characterized by: (1) A gradual stress increase which was linear at first and progressively deviated from linearity closer to failure and (2) sudden stress drops with magnitudes ranging from 4 to 220 MPa (Fig. 1). We observed two different groups of stress drop events: large stress drop (LSD) events with magnitudes between 118 and 220 MPa and small stress drop (SSD) events with magnitudes from 4 to 65 MPa. The characteristics of stress release of the current experiments differ from tests on planar, saw-cut surfaces (Goebel *et al.* 2014) during which predominantly linear stress increases alternated with LSD events. This suggests a direct relation between structural complexity and stress-curve complexity observed before failure, which were present during the current tests on natural-rough, fractured surfaces but absent during saw-cut surface experiments. In Sections 3.2 and 3.3, we examine fault structural complexity and connected changes in AE densities with fault-normal distance and successive stick-slip events in more detail. Periods between successive stick-slip events will be referred to as interslip periods (ISPs). The result section is organized as follows. Initially, we examine generic characteristics of AE hypocentre locations, fault structures, and AE density distributions. We then test changes in AE densities with successive stick-slips exemplified for experiment WG04, and then for all other experiments. Finally, we analyse differences in off-fault AE density distributions between individual experiments and discuss possible mechanisms, for example, differences in fault formation history and fault normal stresses.

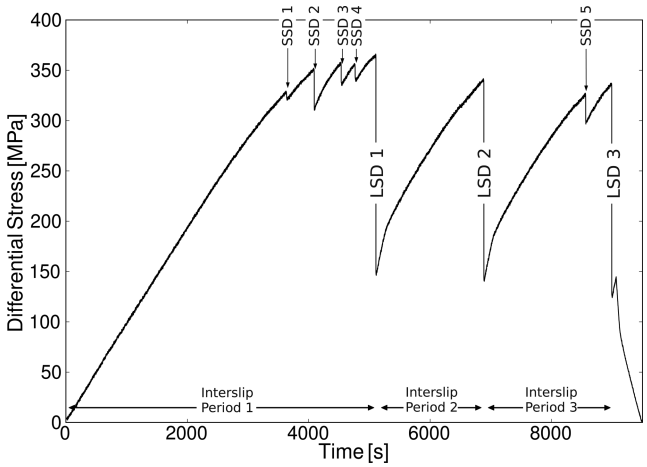

Figure 1. Loading curve for experiment WG04 which resulted in three large stress drop (LSD) events and five small stress drop (SSD) events. The extent of the interslip periods (ISPs) between the LSD events is indicated by black arrows at the bottom of the figure.

3.1 AE hypocentre locations

The observed AE event populations enable monitoring of regions of local failure stress exceedance and connected micro-fracture processes. They also outline the approximate fault-zone extent and orientation within resolution limits and location errors. Fig. 2 shows AE event locations during the three ISPs of experiment WG04, displayed in the corresponding, best-fitting fault coordinate system (X_f, Y_f, Z_f denote coordinates in-plane slip-orthogonal, slip-normal and slip-parallel directions). AE events generally highlight a zone of high strain and brittle deformation, that is, the fault zone that developed from an initial fracture surface. While much of the deformation is localized within a planar zone connecting the two saw-cut notches, we also observed a diffuse zone of AE activity that extended out to larger fault normal distances. Furthermore, the AE event cloud indicates some degree of fault curvature and variations in fault zone widths along the Z_f-axis from 10 to 20 mm. Additional to [*Y*,*Z*] fault curvature, we observed some AE activity towards the

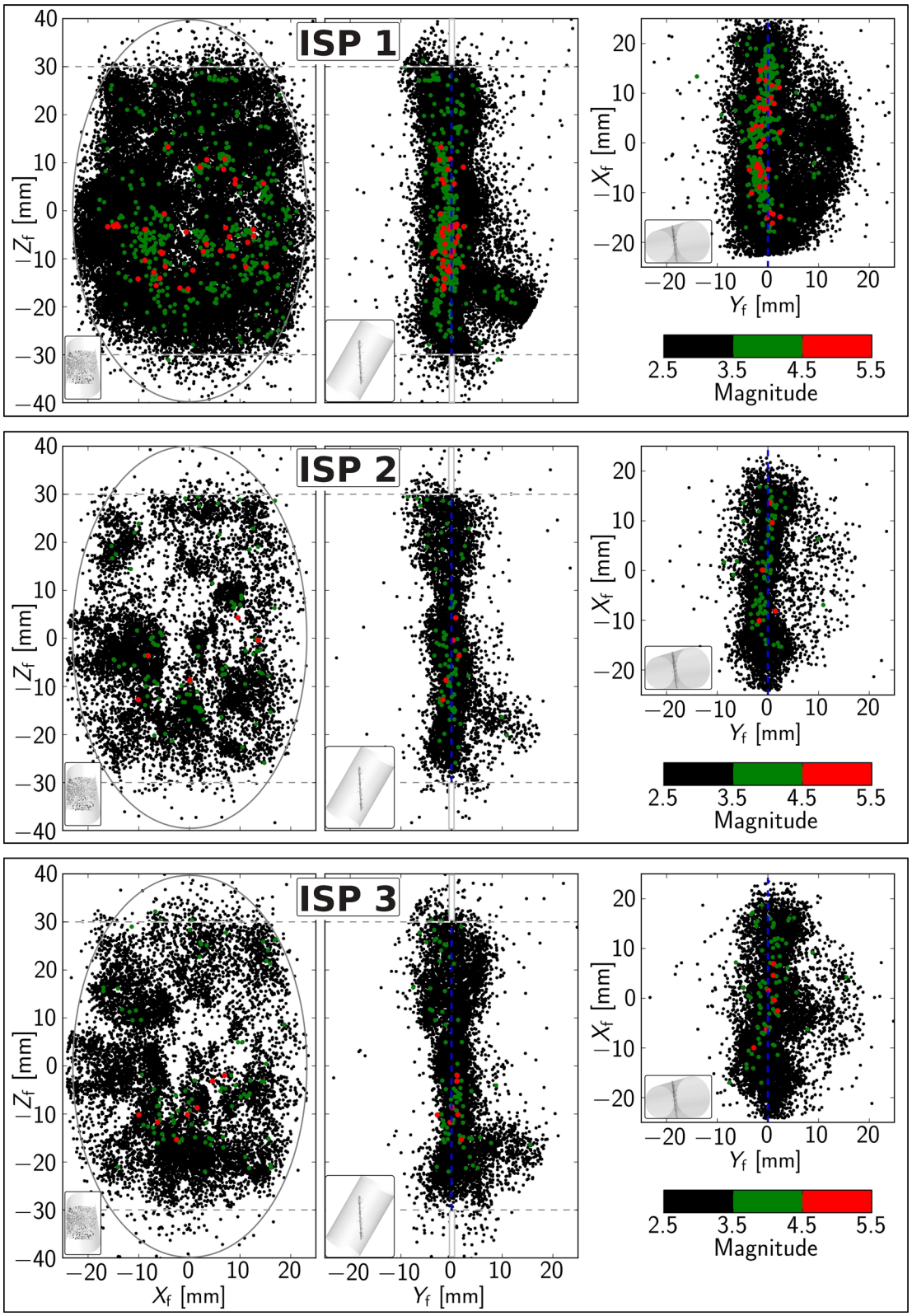

Figure 2. AE hypocentres of experiment WG04 projected into a best-fitting fault coordinate system and viewed in a plane parallel and perpendicular to the fault. Left-hand column: fault-parallel view of AE events. The approximate fault extent is highlighted by a grey ellipse. The grey, dashed lines mark the approximate location of the notch tips. Centre column: AE events within a fault-perpendicular plane (see inset on bottom left-hand side). The extent of the saw-cut notches is indicated by grey bars at the top and bottom. Right-hand column: AE events within a fault-perpendicular plane viewed from the top of the sample. Each row marks a different interslip period of experiment WG04 labelled from ISP1 to ISP3 from top to bottom analogous to Fig. 1. Dots are coloured by magnitude.

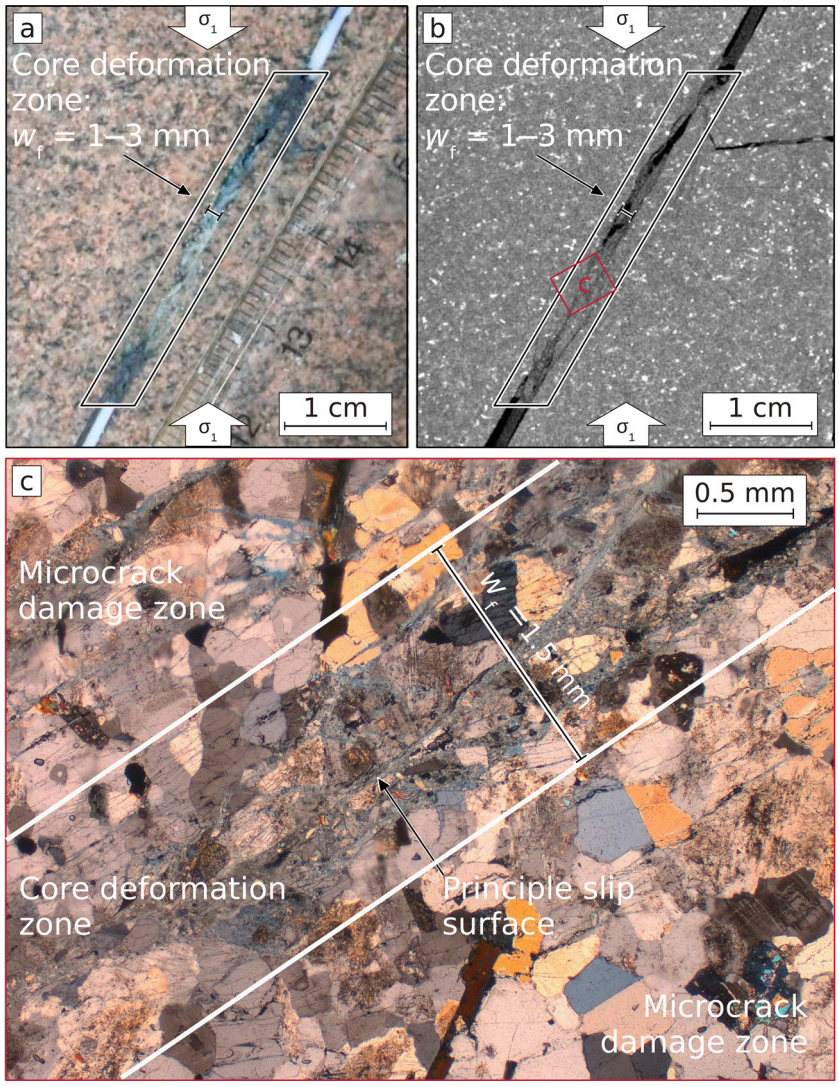

Figure 3. Example of fault zone extent after fracture and subsequent stick-slip sliding during experiment WG07. (a) Photographic image of the centre of the post-experimental fault zone. The width of the core deformation zone (w_f) varied between 1 and 3 mm along the direction of slip. White arrows indicate the direction of maximum compression. (b) CT-scan of the same fault area as in (a). Black, linear features highlight extent of core deformation zone that consists of sets of anastomosing cracks. The CT-scan images confirmed a core deformation zone width between 1 and 3 mm. The large crack outside of the core deformation zone (upper right) was formed early during the experiment and was active only during initial periods. (c) Microscopic image of thin section of the red rectangular region highlighted in (c). The core deformation zone contains ultrafine-grained gouge, larger clasts and pervasive microcrack damage, as well as one or more principle slip zones. The minimum width of the core deformation zone was between 1 and 1.5 mm. Outside of this zone, we observed a network of microcrack damage that was present in most of the thin section.

sample boundary [($Z_f = -20$ mm, $Y_f = 15$ mm) in the upper frame of Fig. 2] likely connected to secondary faulting. The highest AE activity was observed during the first ISP whereas later ISPs showed less activity and more pronounced AE clustering within localized fault regions.

3.2 Fault structure and average AE density distributions

In the following, we investigate fault structural characteristics and damage-zone widths inferred from post-experimental microstructure images and fault-normal AE event density distributions, exemplified for experiment WG07. Thin-section images of the laboratory-created fault zones revealed zones of highly strained material within the fault core consisting of fault gouge, larger clasts (up to ∼0.1 mm) and one or more principle slip surfaces. These zones are embedded into highly fractured host rock. The density of micro fractures decreased as function of distance from the core deformation zone (see also Goebel *et al.* 2013b). The width of the core deformation zone could be identified within individual fault-orthogonal planes in photographic and CT images (Figs 3a and b), revealing strong variation along fault-strike. The maximum extent is up to ∼3 mm but may also be higher if additional principal slip surfaces are present. Principal slip surfaces, which have estimated widths on the order of tens of micrometres, exhibit a complex behaviour: diverging and joining together in different fault regions enclosing larger clasts between anastomosing branches. The enclosed material is commonly strongly fractured and shows local evidence of shear. The minimum extent of the core deformation zone was ∼1 mm (Fig. 3c), however, this width is also difficult to constrain due to the inherent incompleteness of 2-D representations of a 3-D, structurally complex fault zone. Thus, the

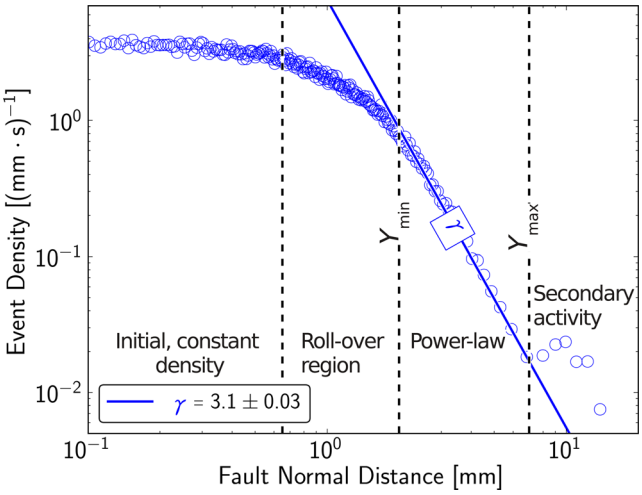

Figure 4. Example of AE density distribution (blue circles) as function of fault-normal distance for experiment WG07. The blue line depicts the fit of the power-law distributed data between the power-law bounds marked by Y_{min} and Y_{max} (vertical, dashed lines).

minimum width may even be lower in zones of highly localized deformation. Moreover, the displayed fault structure is the result of sample fracture and subsequent stick-slip events. The initial fault creation may already produce some microcrack damage within the fracture process zone (Vermilye & Scholz 1998; Janssen *et al.* 2001). Thus, the post-experimental structural analysis provides a cumulative picture of the created damage rather than resolving damage caused by individual stick-slip events.

To obtain a more detailed picture of stick-slip related damage, we tested a possible connection between fault structure and average AE density distributions. The latter were initially estimated for AE events of all ISPs. Events within a 8–20 s time window after slip onsets, showed a pronounced Omori-type aftershock decay (Goebel *et al.* 2012, 2013b). The aftershocks together with AE events that were associated with slip events were excluded from the current analysis because, here, we are interested in damage creation during stress increase on rough faults.

AE densities were determined using the same sample size ($N = 30$) for all experiments to ensure comparability of the results. We tested different values for N ranging from 10 to 240 which resulted in varying degrees of smoothness of density distributions and a slight decrease of the maximum extent of AE densities for the largest values of N, while the rate of special decay of AE densities remained largely unchanged (see Fig. S2). The AE density in our experiments was generally high close to the fault axis and remained at approximately constant values out to distances of several millimetres, for example, ∼2 mm for WG04 (Fig. 4). The constant, high AE activity indicates strong brittle deformation within this zone. At larger distances, the AE-density decay could be described by a power law. The power laws were bounded by the parameters Y_{min} and Y_{max} (see Fig. 4). The former marks the transition between high AE activity within the core deformation zone and the power-law decay in AE activity. Y_{max} marks the transition to a zone of secondary, seismic activity. This activity is likely not directly connected to the deformation along the fault but could rather be caused by large secondary cracks, or pre-existing material heterogeneity. In our experiments, quantitative estimates of Y_{max} are impossible if the transition to the secondary activity occurs at large distances, or if the secondary activity is low. Consequently, the following analysis and interpretation are largely based on the power-law exponents, γ, and the minimum bounds, Y_{min}, which can be estimated more reliably. In addition, we determined the parameters γ^* which shows the variation in γ as a function of different values for the lower power-law bound, and γ_s which is the power-law exponent corrected for hypocentral uncertainties.

Table 2. Width of core deformation zone (w_f) estimated from post-experimental CT-scans, thin sections, and photographic images as well as lower bound (Y_{min}) and exponent (γ) of power-law distributed AE densities. l_{RS} is the length of the rough fracture surfaces.

Sample	w_f (mm)	Y_{min} (mm)	l_{RS} (cm)	γ	p-Value
WG04	1–4.2 ± 1	3.8	5.0 ± 0.15	3.2 ± 0.07	0.18
WG05	1–4 ± 1	0.9	4.2 ± 0.15	1.9 ± 0.01	0.15
WG07	1–3 ± 1	2.0	3.7 ± 0.15	3.1 ± 0.03	0.45
WG08	0.5–2.5 ± 1	1.6	3.0 ± 0.15	2.1 ± 0.02	0.11

The core deformation zone widths, w_f and the minimum power-law bound, Y_{min}, varied systematically with the length of the saw-cut-guided, fracture surface, l_{RS} (Table 2). Longer, rough surfaces were generally connected to larger maximum values of w_f. Similarly, Y_{min} increased as a function of l_{RS} for all experiments, except for WG05. The increase in Y_{min} highlights that longer, initially rough surfaces led to broader damage zone widths and broader zones of high AE activity. Experiment WG05 showed lower values for both power-law exponent, γ, and Y_{min} than expected from the corresponding values of l_{RS} and w_f, which will be explored in more detail in Section 3.4.

The width of the zone of high AE activity, which is approximately $2Y_{min}$ because of the profile stacking from both sides of the fault, is generally wider than the estimates of w_f. This difference in width can be explained by a previously identified lower resolution between optical and AE methods (Zang *et al.* 2000). Optical methods generally have a lower resolution so that the AE hypocentre locations resolve damage structures out to larger fault-normal distances. Nevertheless, the initial comparison between fault zone structure and fault-normal AE density distributions shows interesting parallels, for example, the pronounced zone of high brittle deformation seen in both the microscopic images and high AE event densities close to the fault axis. This zone transitions into a power-law fall-off in AE densities and a region of decreasing microcrack densities observed in thin-section images.

3.3 Changes in density distributions and off-fault activity exponents with successive stick-slip events

We explored variations in the spatial decay of AE density distributions with successive ISPs starting with experiment WG04. The initial ISP of experiment WG04 showed a plateau of AE density close to the fault axis out to a distance of about 2 mm (Fig. 5, top panel). Further out, a roll-over region occurs between 1.5 and 2.3 mm, and a power-law decay out to distances of $Y_f \sim 7$ mm. Secondary AE activity was also visible but did not influence the power-law slopes close to the fault. This observation was confirmed by computing power-law exponents without the region of secondary cracking. The power-law exponents increased systematically with successive stick-slip events, that is, a relatively larger proportion of AEs appeared closer to the fault highlighting a faster spatial decay during later ISPs (Fig. 5).

To investigate the characteristics of individual density distributions in more detail, we computed the power-law exponent, γ^*, as function of varying minimum power-law cut-offs, Y^*_{min} (Fig. 5, insets). In case of power-law distributed data, we expect to observe

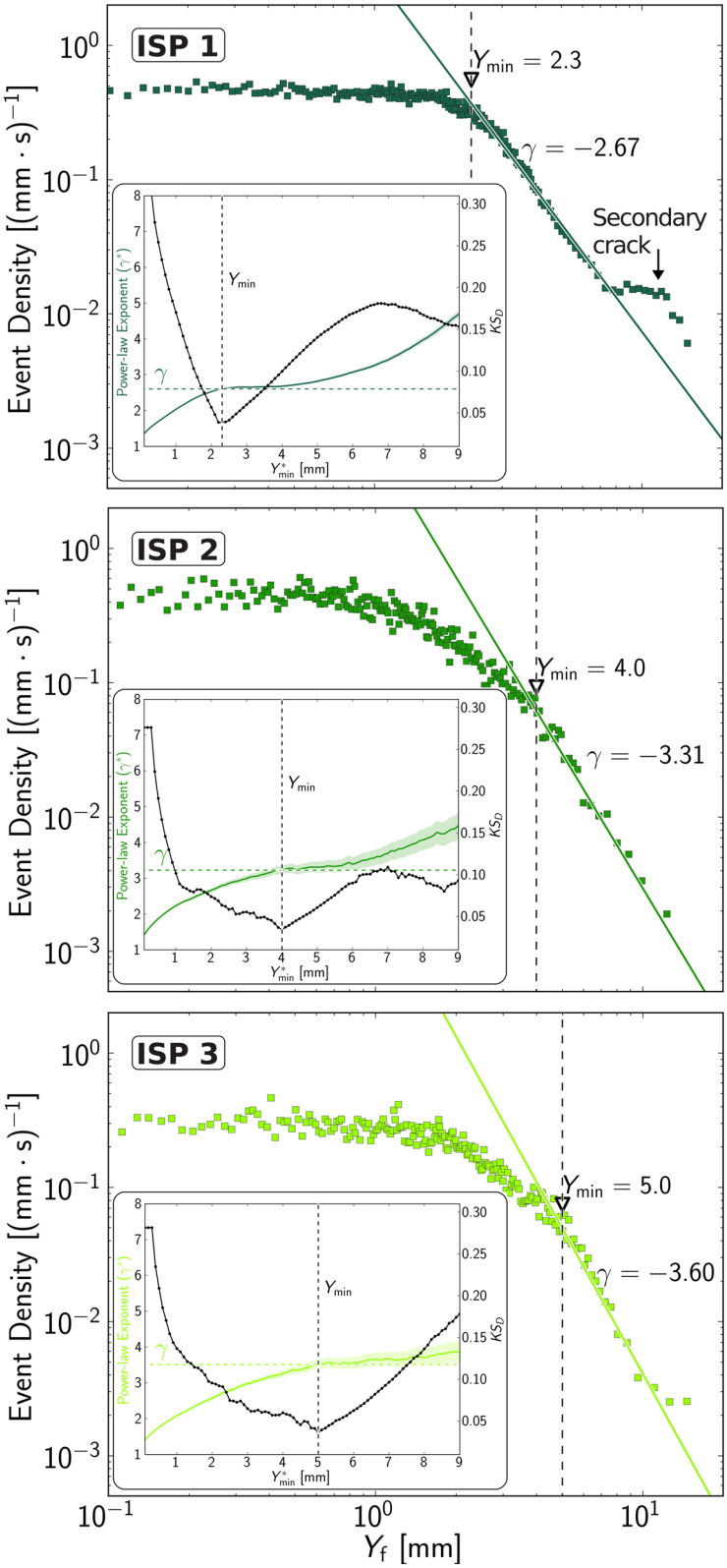

Figure 5. AE event density as function of fault-normal distance for the three ISPs of experiment WG04. Power-law exponents are displayed next to the straight solid lines in each frame and minimum bounds of the power laws are highlighted by triangles. The insets show changes in γ for different values of Y_{min} and the corresponding KS-distances, that is, the minimum between distances between modelled and observed distributions (see text for details). The best-fitting Y_{min} value (black dashed lines in inset) minimizes the KS-distance. The corresponding γ-values are marked by horizontal, coloured, dashed lines within the insets.

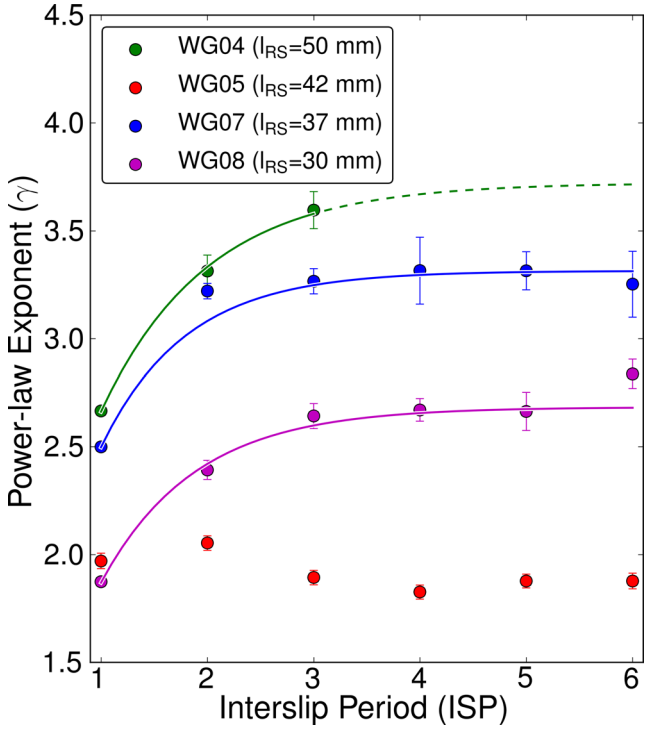

Figure 6. Changes in off-fault activity exponent (γ) with successive stick-slip events. Markers are coloured according to different experiments. The solid lines are trend lines highlighting the initial rapid increase in γ followed by approximately constant values. The green dashed line represents an extrapolation for experiment WG04 using an exponential function of the form: $\gamma = A - B\exp(-Cn)$, where A, B and C are empirical fitting parameters, and n is the respective ISP.

a rapid increase in γ^* below Y_{min}, followed by largely constant values over the extent of the power law and larger fluctuations in the distribution tail. The corresponding KS-distances for different values of Y^*_{min} show a minimum at the beginning of the γ^*-plateau in agreement with the expected Y_{min} values (Fig. 5, inset). The γ^* values increased systematically over the whole range of Y^*_{min} with subsequent ISPs emphasizing the robustness of the evolutionary trend. The range of the power-law behaviour remained approximately constant over the series of stick-slips based on an assessment of the constant portion of γ^*. Y_{min} increased systematically with successive stick-slip events from 2.3 for ISP 1 to 4 for ISP 2, and 5 for ISP 3. The uncertainties in γ are generally small, compared to those in Y_{min} which showed uncertainties up to ~0.5 mm due to the extended roll-over regions. The lower bound, Y_{min}, is an important parameter in distinguishing the power-law distributed, off-fault activity, and the 'on-fault' activity which consists of regions of constant AE density and is bounded by the roll-over region. For simplicity, we will refer to AE events that occurred at fault-normal distances above Y_{min} as off-fault, and those below as on-fault activity.

We examined if the observed trend of decreasing off-fault activity exponents could be observed for all experiments (Fig. 6). Experiments WG04, WG07, and WG08 show a similar relative trend in γ, that is, comparably low values at the beginning, followed by an increase over the initial 1–3 ISPs. All experiments approached approximately constant values during later ISPs. We observed a substantial difference in the average value of γ between the experiments. Experiment WG05 showed the lowest average γ-value, and also deviated from the previous trend of initial increasing power-law exponents and subsequent constant values. The other experiments showed increasing average values of γ with increasing length of the rough fault zones. In the following, we investigate experiment WG05 in more detail by comparing it to experiment WG07. Both experiments had similar initial sample geometries (i.e. length of saw-cut notches) and were subject to similar loading stresses.

In spite of similar initial sample geometry, the natural fracture process of the intact part between the ends of the notches resulted in varying fault structure and fault orientation for different experiments. These differences are also expressed in variations of the principal orientation of AE hypocentre populations. In the following, we assume that AE hypocentre locations are connected to principle slip surfaces so that the regions of highest AE densities mark the locations of the principle slip surfaces. Consequently, we can determine possible variations in slip surface orientation for each ISP by projecting the AE hypocentres into a best-fitting fault coordinate system. The corresponding fault angles, μ_f, are used to compute changes in normal stress with successive ISPs and between experiments.

Normal stress and μ_f vary substantially between WG05 and WG07 (Fig. 7). For experiment WG05, the best-fitting fault plane was oriented at ≈40° angle from the vertical loading axis during the initial ISP. This angle decreased systematically with successive stick-slip events down to $\mu_f \approx 35°$ during the last ISP. Experiment WG07, on the other hand, showed an approximately constant fault orientation at $\mu_f \approx 27°$ (see Fig. S5). In addition to changes in μ_f, we observed that WG05 showed substantially higher AE activity than WG07 at larger distances from the fault surface. This difference is in agreement with the average values of γ.

To further test for possible differences in fault orientation, fault structure, and changes in principle slip surfaces between WG05 and WG07, we analysed post-experimental CT images (Fig. 8). The CT-images generally depict the cumulative damage creation due to sample fracture and subsequent stick-slip events. The CT-scans revealed slightly larger fault angles for WG05 compared to WG07. Furthermore, we observed a comparably broad zone of high crack-density for experiment WG05 whereas WG07 showed a more localized core deformation zone (Fig. 8 insets). To compare these results to our prior estimates of μ_f, we highlighted the corresponding angles in both CT-images. The damage-zone orientation and width within the CT-scan of experiment WG05 highlight a likely migration of the principle slip surface from 40° to 35° during successive stick-slip events. The damage-zone width of WG07, on the other hand, is comparably narrow, underlining the pronounced stability of principal slip surface orientations and μ_f. Our estimate of μ_f based on AE hypocentres was ≈1° lower than expected from CT-images, but is in agreement with a possible range of $\mu_f = 27°–30°$ based on the observed width of the fault zone in Fig. 8. Due to the cumulative character of the damage within the CT-images a precise estimation of the fault angles for each ISP is complicated. Nevertheless, the slightly larger angle between fault and loading axis for experiment WG05 together with the broader damage zone support the previously suggested differences in μ_f between WG05 and WG07.

3.4 Changes in off-fault activity exponent with normal stress

Based on the variations in fault angle and the relatively large differences in effective, rough surface area (i.e. the fault area between

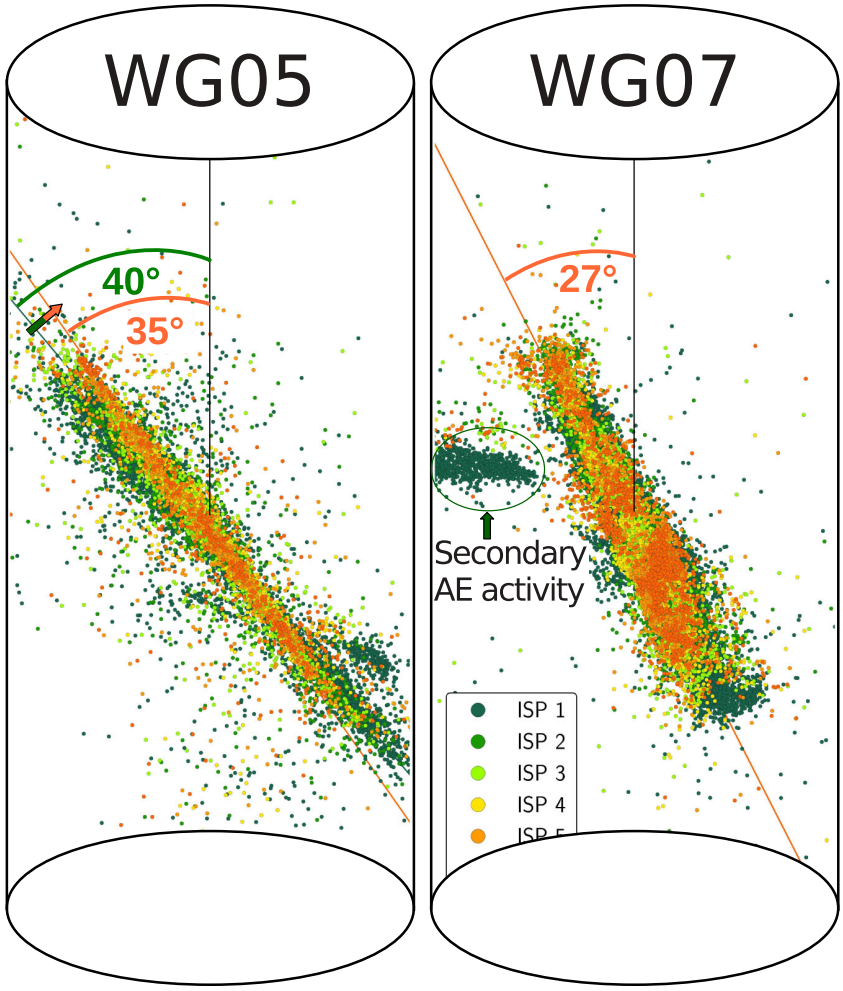

Figure 7. Changes in fault orientation inferred from AE populations for experiment WG05 (left) and WG07 (right). The marker-colours correspond to AE events recorded during the individual ISPs of an experiment. WG05 had relatively larger fault angles which decreased with successive stick-slip events whereas WG07 had an approximately constant angle of 27°. Experiment WG07 displayed some AE activity related to secondary faulting below the end of the upper notch (green ellipse).

the pre-cut notches), we also expect the stress level on the faults to differ between experiments. To investigate the influence of normal stress on seismic off-fault activity, we computed shear and normal stresses (see Table 1) corrected for both notch lengths and fault displacements. We then compared stress estimates to average off-fault activity exponents. To this aim, we compiled the AE events of all ISPs and computed AE density profiles but again excluded events within initial ISPs which showed the strongest deviation from the average γ values. We observed a general trend of lower off-fault activity exponents with increasing normal stress so that γ and σ_n show a negative, linear relationship (Fig. 9). The corresponding Pearson's correlation coefficient was estimated at $r = -0.93$ (Spearman's rank $= -0.80$). Larger normal stresses result in a relatively larger proportion of off-fault activity which are associated with the relatively low γ-values, for example for experiment WG05, which experienced the largest fault stress level and a comparably slow off-fault activity decrease.

Table 3 presents an overview of off-fault activity exponents, corresponding goodness-of-fit (p-values) and the AE rate for individual experiments. In Goebel *et al.* (2014), we investigated the influence of hypocentral uncertainties on power-law parameters of the off-fault activity decay, and we find a linear increase in both γ and Y_{min} as function of hypocentral uncertainty, if the latter follows a normal distribution. The power-law exponents, γ_{corr}, corrected for hypocentral uncertainties, are displayed in Table 3, as well as in Fig. 9 assuming an average hypocentral uncertainty of ∼2 mm, and are the basis of the following discussion.

4 DISCUSSION

4.1 Relating fault structure and AE density distribution

Our results suggest a close connection between fault structure and AE density distributions. The density distributions are characterized by a zone of constant, high AE density close to the principal slip surface, a roll-over region, and a zone of rapid activity decay which could be described by a power law. Within a previous experimental series, we showed that the power-law decay is controlled by both fault roughness and fault normal stress (Goebel *et al.* 2014). Through analysing sets of post-experimental thin-sections, we quantified the connection between fault structure and resulting AE density characteristics (Fig. 10). The high AE density plateau is connected to strong brittle deformation within the fault core which is dominated by fine-grained gouge, large, elongated clasts (up to ∼0.1 mm) and zones of localized slip. We observed a

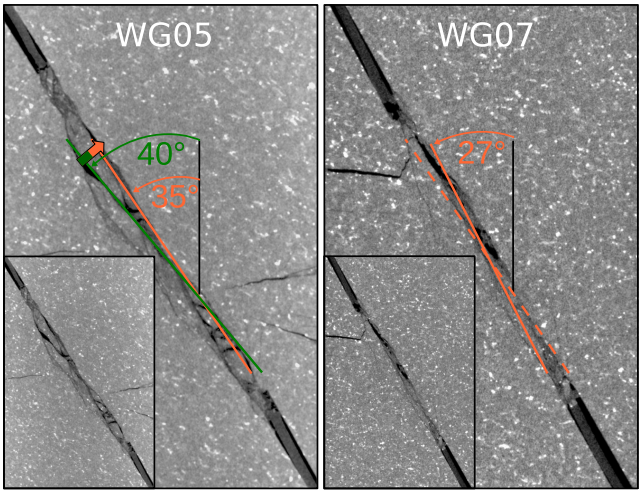

Figure 8. Fault structure and orientation in post-experimental computer tomography scans of experiments WG05 (left-hand side) and WG07 (right-hand side). The fault angles are highlighted by solid green and orange lines. For a comparison, we also highlighted a 35° angle for experiment WG07 (orange, dashed line). The insets show the fault structure without marked fault angles. The saw-cut notches filled and inserted teflon sheets are visible to the upper left and lower right of each image.

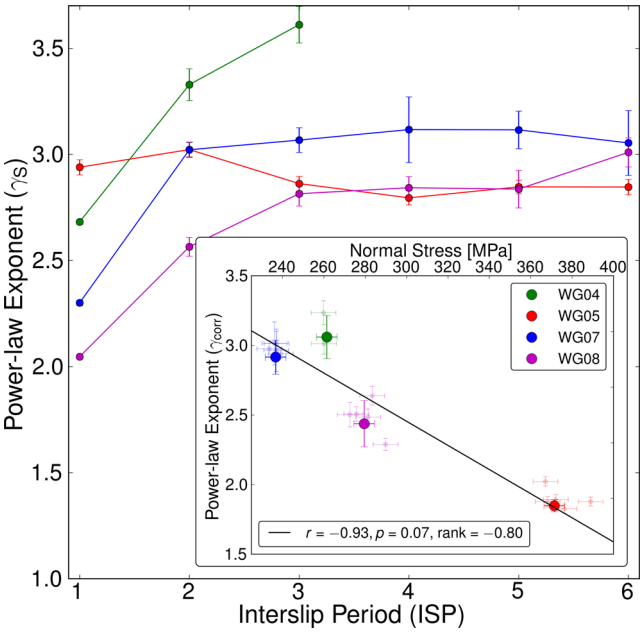

Figure 9. Off-fault activity exponent (γ_s), corrected for hypocentral uncertainty, and normal stress. We observed an inverse, linear relationship between γ_{corr} and σ_n (inset). The larger markers within the inset depict average values of γ_{corr} for later ISPs and the smaller markers show value for individual ISPs. Pearson's correlation coefficient, p-value and Spearman's rank are displayed in the lower left of the inset. We used this relationship to correct the different values of γ in Fig. 6 for different normal stress level, expectedly, resulting in a partial data collapse within narrow range of exponents.

transitional damage zone between highly deformed fault core and host-rock that showed pervasive fracturing and evidence of local shear deformation. Progressive damage accumulation likely led to a widening of the transitional damage zone as well as an increase in Y_{min} (see Fig. 5). A widening of the damage zone may occur in form of wall rock erosion, grain fracture, grain plucking and subsequent assimilation into the central gouge layer (e.g. Amitrano & Schmittbuhl 2002). However, these observations should be interpreted cautiously because both roll-over zone width and Y_{min} are sensitive to hypocentral uncertainties and small variations during the projection of AEs into the corresponding fault coordinate systems.

4.2 Mechanisms of power law distributed off-fault activity

We observed a systematic change in γ with increasing normal stress and successive stick-slips. The latter highlights the connection between off-fault activity, and fault evolution in form of roughness reduction with larger displacement. The influence of roughness and normal stress on the off-fault activity can be understood within the context of varying asperity-size distributions on material interfaces: Higher normal stresses on rough faults result in an increase in effective contact area and a relative higher proportion of large asperities (Dieterich & Kilgore 1996; Goebel *et al.* 2014). In addition, variations in fault roughness strongly influence the spatial decay of off-fault stresses (Dieterich & Smith 2009), and thus also the spatial decay of AE activity, if stress is mainly released seismically. Fault roughness and seismic off-fault activity are related through the following equation (Dieterich & Smith 2009; Powers & Jordan 2010; Goebel *et al.* 2014):

$$\gamma = c_g - H, \tag{1}$$

where c_g is the geometric dimension, and H is the Hurst exponent of a fractal rough fault (see e.g. Mandelbrot 1982; Turcotte 1997). Goebel *et al.* (2014) noted that this is a more general form of the initially suggested model by Dieterich & Smith (2009), that accounts for the difference in asperity shapes and corresponding stress perturbations in 3-D. In 3-D, stress decays with distance (r) from an asperity as $1/r^3$ as opposed to $1/r^2$ in 2-D. Consequently, we expect the off-fault activity exponent to vary between 2 and 3 corresponding to Hurst exponents between 0 and 1 (Eq. 1). This expectation is approximately met by our observations (e.g. Fig. 11), although γ may reach values below 2 for rough faults that are loaded at high normal stresses. Surfaces with Hurst exponent of $H = 1$ are connected to a relatively larger proportion of roughness at large wavelengths compared to surfaces with $H = 0$ which show a larger proportion of roughness at small wavelengths.

4.3 Fault smoothing and the influence of normal stress and fault formation history

Our results show that fault evolution is complex even on incipient fracture surfaces in the laboratory. This complexity arises due to the interplay of fault roughness, stress and fault formation history. Changes in off-fault activity exponents, which were characterized by an initial increase over the first 1–3 ISPs, indicate strong fault smoothing at the beginning of the experiments. This is in agreement with a previous study during which we inferred a strong initial reduction in fault complexity based on decreasing fractal dimensions of AE hypocentre distributions (Goebel *et al.* 2013b). In that study, we observed fractal dimensions to decrease from initial values of 2.5 down to values close to 2. The latter is consistent with a predominantly planar distribution of AE hypocentres in 3-D and progressive fault smoothing. Fault smoothing is likely associated with the formation of zones of localized slip. These zones, which form after as little as 1–3 stick-slip events, were also observed in post-experimental

Table 3. Overview of off-fault activity and AE rate for the four experiments. γ: off-fault activity exponent, γ_{ave}: average power-law exponent and standard deviation for all ISPs except the initial ISP, γ_{corr}: power-law exponent corrected for hypocentral uncertainty, p-value: goodness-of-fit of estimated γ-values, computed by Monte Carlo resampling, of the modelled distributions and comparing them to the observed distributions (Clauset *et al.* 2009). Within the scope of this study, we consider a power law a valid hypothesis for p-values above 0.10. N_{AE}: total number of AE events, N_{AE} s^{-1}: number of AE events per second.

Sample	γ	γ_{ave}	γ_{corr}	p-Value	N_{AE}	N_{AE} s^{-1}	N_{LSD}	N_{SSD}
WG04	3.37 ± 0.15	3.45 ± 0.14	3.06 ± 0.14	0.21	17,363	4.58	3	5
WG05	1.84 ± 0.10	1.91 ± 0.08	1.84 ± 0.08	0.11	20,020	4.24	6	5
WG07	3.19 ± 0.12	3.27 ± 0.04	2.92 ± 0.08	0.18	27,797	3.51	6	8
WG08	2.58 ± 0.17	2.54 ± 0.09	2.44 ± 0.08	0.29	17,890	2.45	6	5

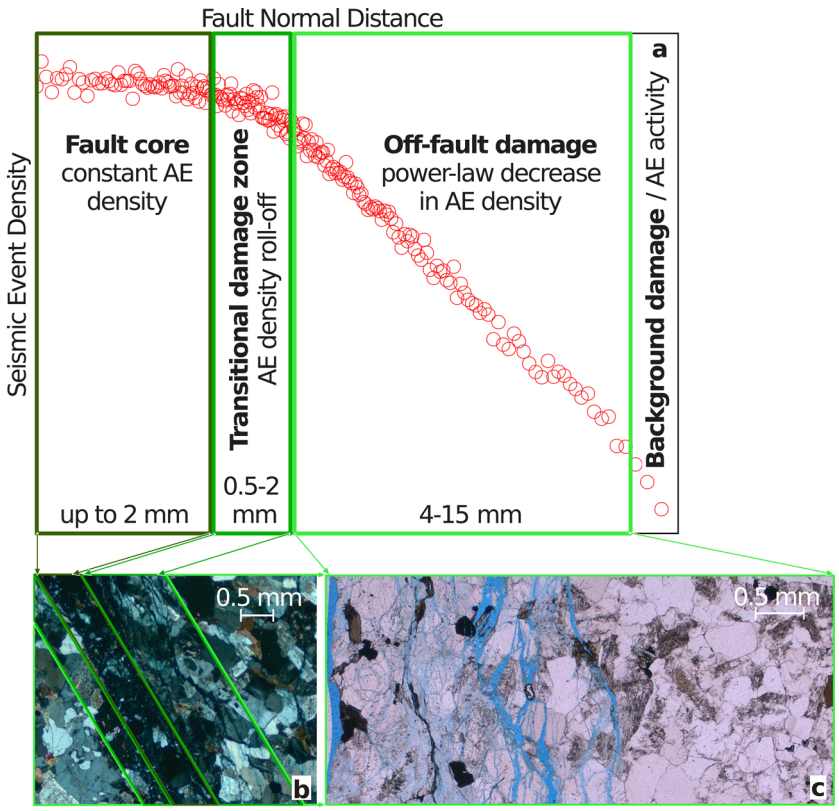

Figure 10. Connection between fault structure and across-fault AE density profiles. a): AE density distribution displayed on double logarithmic scales (red circles). The fault core is connected to a constant AE density, which is followed by a transitional zone over which the AE density decreases gradually, as well as the off-fault damage zone which is characterized by a power law decrease in AE density and lastly, the background damage which is the source of the background AE activity. b): Thin-section of fault core consisting of highly fractured grains and gouge, and the transitional damage zone with highly damaged material that shows evidence of localized shear deformation (see also Fig. 3c). c): Thin-section of off-fault damage zone. Loose particles and gouge were removed. Micro-cracks are highlighted in blue.

thin-sections (e.g. Fig. 3). Within the present study, we observed a reduction in secondary cracking and associated AE activity with successive stick-slip events (see e.g. Fig. 5) indicating that off-fault damage seems to also progressively localize.

Experiment WG05 deviated from the other three experiments by showing consistently low γ-values and lacking the initial periods of fault smoothing. This could be explained by an interplay of fault formation and evolution effects: The freshly formed fracture surface for this experiment was connected to a comparably large fault angle which changed gradually with successive stick-slip events. The preferred fracture angle of Westerly granite is between 25–30 $^{\circ}$ (e.g. Mogi 2007), which is in agreement with our experiments except for experiment WG05 (see Fig. S5). The fracture process of experiment WG05 may have been influenced by material heterogeneity or slight deviations in orientation and width of the saw-cut notches leading to γ-values which are higher than expected. The systematic changes in fault angle after the initial fracture process are likely related to changing slip surface orientations and a more favourable alignment with the principal stresses. Moreover, for this experiment, we observed a relatively wider damage-zone and large-wavelength anastomosing crack structures in post-experimental thin section and CT scans. The extent of the damage zone may be connected to repeated variations of principle slip surface orientations. Thus, a combination of initial fault zone orientation, and changes in fault zone structure due to stick-slip fault motion are likely responsible for the observed differences in characteristics of AE density distributions.

Goebel *et al.* (2014) observed that increasing fault normal stresses result in a decrease in γ for experiments on rough saw-cut surfaces. We compare these results with values of γ_{corr} from initial ISPs of the

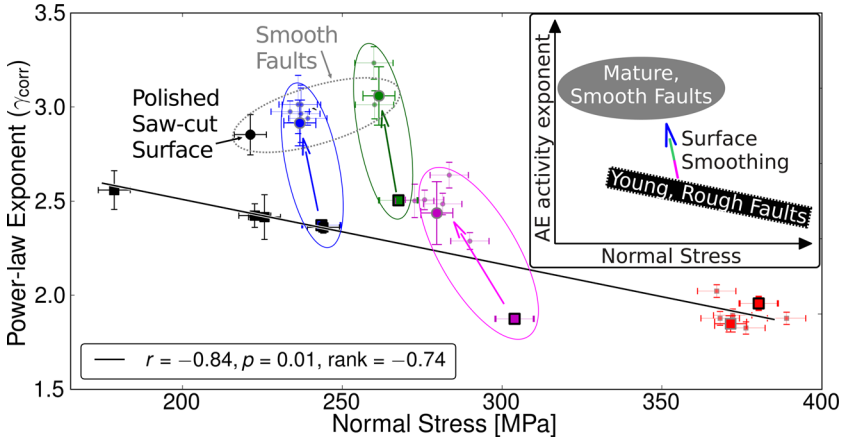

Figure 11. Compilation of off-fault activity exponents corrected for hypocentral uncertainty (γ_{corr}). We show results of experiments on saw-cut surfaces with predefined roughness (Goebel *et al.* 2014) as well as complex fault zones that developed from incipient fracture-surfaces (this study). The black symbols represent results from the saw-cut experiments: black squares are relatively rough surfaces whereas the black circle (upper left) is from an experiment on a polished surface (for details, see Goebel *et al.* 2014). The coloured symbols represent the fractured surface experiments: The coloured squares are γ_{corr}-values during initial ISPs; round, coloured symbols are average γ-values; and the small coloured markers show γ_{corr} during individual ISPs (colours are the same as in Fig. 9). The off-fault activity exponents of the relatively rough surfaces (both saw-cuts and fractured surfaces) follow an inverse linear relationship with normal stress (dark solid line, slope $= 3 \times 10^{-3}$MPa^{-1}). The fractured surface experiments evolve towards slightly lower peak stresses and higher γ values with successive stick-slip events (coloured ellipses and arrows), except for experiment WG05. The inset depicts a schematic diagram of fault evolution within based on laboratory-created fault zones.

current experimental series (Fig. 11). The two sets of experiments, including experiment WG05, can be described by a negative, linear relationship between γ_{corr} and σ_n (see squares and solid black line in Fig. 11). This relationship highlights the sensitivity of rough surfaces to variations in normal stress so that larger normal stresses generally lead to a slower spatial decay of AE events with respect to the fault axis. Besides the influence of normal stress, Fig. 11 also displays the evolution of laboratory faults with successive stick-slip events. Within the first 1–3 ISPs, the γ_{corr}-values increased rapidly (coloured ellipses in Fig. 11) reaching values similar to that of a smooth, polished surface (grey, dashed ellipse in Fig. 11). This similarity between γ_{corr} of relatively mature, fractured surfaces and polished saw-cut surfaces may also imply similar fault roughness. Consequently, the repeated rupture of natural rough surfaces over series of stick-slip events is likely connected to extensive surface smoothing, so that mature, gouge-rich faults show similar AE density decays to fresh, polished surfaces with little to no displacements. Based on the current set of experiments, we cannot resolve how generic the observed smoothing processes are, raising the question, whether all natural-rough surfaces eventually evolve into smooth faults, characterized by localized slip and decreasing spatial extents of off-fault activity.

Fault smoothing rates likely depend on the formation history and stress state of the fault. Roughness reduction may be most effective within a certain range of conditions, for example, high initial roughness and favourable alignment with the principle stress axes. The difference in the smoothing process is most easily seen for experiment WG05 which showed no evidence of fault smoothing within the present range of displacements. The current experimental series are limited to comparably small displacements and we cannot rule out that secondary smoothing processes will become active or observable after sufficient displacement has been accumulated. Despite these limitations, we observe many similarities between the statistics of AE events and natural seismicity. This highlights the importance of our results for the understanding of seismicity variations in nature.

4.4 Is fault evolution limited to small displacements?

A power-law decay in seismic off-fault activity is in agreement with a theoretical study Dieterich & Smith (2009) and a study of the spatial decay of seismicity in the proximity of natural faults (Powers & Jordan 2010). Powers and Jordan suggested that off-fault activity exponents decrease systematically with increasing displacements and fault smoothness even at large displacements of up to 300 km. Our results support progressive fault smoothing with successive stick-slip events, however, this process may not be continuous. Within the range of displacements of the current experimental series, we observed that faults rapidly reached an approximately constant value of γ suggesting that roughness remained at a stable level thereafter. Similar observations have been made for exhumed crustal fault zones, for which a reduction in roughness and extension of damage zone widths are predominately active within the first 10–100 m of cumulative fault displacements whereas above no evolutionary signal is observable (Sagy *et al.* 2007; Savage & Brodsky 2011; Brodsky *et al.* 2011). On the other hand, a reduction in fault stepovers and geometric disorder is observed even for faults with large cumulative displacements (e.g. Wesnousky 1988; Wechsler *et al.* 2010) suggesting that evolutionary processes are active on mature faults.

The differences between laboratory and natural seismicity can possibly be attributed to additional complexity in structure and roughness of natural fault zones. Most of the off-fault activity exponents of natural seismicity fall within a range of 1–2 (Hauksson 2010; Powers & Jordan 2010). Powers and Jordan noted that this range of exponents is consistent with theoretical results for seismic off-fault activity in the proximity of fractal, rough faults in 2-D for which $\gamma = 2 - H$ (Dieterich & Smith 2009). However, as pointed out in Goebel *et al.* (2014), in 3-D one expects the seismic off-fault activity to be related to the fractal roughness over $\gamma = 3 - H$. The roughness of natural faults may be controlled by depth persistent structural features like fault stepovers. These stepovers likely introduce a roughness component that is approximately constant with

depth and changes only along strike thus influencing the off-fault seismicity decay similarly to a fault in 2-D. Hence, fault-normal seismicity distributions are likely influenced by both surface roughness and structurally induced roughness which may explain the entire range of γ-values including high values of up to $\gamma = 3$ in Powers & Jordan (2010). This influence may also explain the apparent discrepancy between studies that propose fault smoothing to be continuous versus studies that propose smoothing to only be active at small displacements. Moreover, our experiments highlight the role of increased normal stresses which cause faults to appear 'seismically rougher', that is, they are characterized by a slower spatial decay of seismic off-fault activity.

5 CONCLUSION

We conducted four frictional sliding experiments on rough fault zones that evolved from incipient fracture surfaces. The laboratory-created faults showed many similarities to natural fault zones including a core deformation zone consisting of gouge and areas of slip localization as well as an off-fault damage zone with decreasing crack density at increasing fault-normal distances. We observed a connection between the characteristics of seismic-event density distributions and the structure of complex, laboratory-created faults. The core deformation zone was associated with consistently high AE activity whereas the off-fault damage zone showed a power-law AE density decay. The exponent of this power law is sensitive to normal stress and changes in fault roughness, and can be used to document fault evolution with successive stick-slip events.

The laboratory faults showed strong evidence for fault evolution during the initial 1–3 interslip periods as a consequence of fault smoothing and reduction in fault complexity. Over the following interslip periods, fault evolution was no longer observable based on variations in off-fault AE distributions. The lack of evolutionary signals suggests that fault smoothing processes are most effective during early stages of fault development. Relative differences in off-fault activity exponents between experiments were predominantly controlled by the normal stress on the faults revealing a linear relationship between normal stress and off-fault activity exponents for rough faults. Consequently, increasing normal stresses generally result in a relatively slower spatial decay of seismic off-fault activity.

Our results highlight that fault roughness, stress state, and formation history of a fault are important parameters that control near-fault seismicity distributions. Distinguishing between roughness- and stress-related variations in fault-normal distributions of natural seismicity may provide important insights into fault zone properties including along strike variations of frictional properties and stress.

ACKNOWLEDGEMENTS

We thank Stefan Gehrmann and Matthias Kreplin for the rock sample preparation at GFZ-Potsdam, Germany. The authors wish to thank the editor, Jörg Renner, and two anonymous reviewers for suggestions that helped improve an earlier version of the manuscript. This research was supported in part by the Southern Californian Earthquake Center under contribution numbers 11017 and 13022.

REFERENCES

Amitrano, D. & Schmittbuhl, J., 2002. Fracture roughness and gouge distribution of a granite shear band, *J. geophys. Res.,* **107,** 1–19.

Ben-Zion, Y. & Sammis, C.G., 2003. Characterization of fault zones, *Pure appl. Geophys.,* **160,** 677–715.

Bhat, H.S., Dmowska, R., Rice, J.R. & Kame, N., 2004. Dynamic slip transfer from the Denali to Totschunda faults, Alaska: testing theory for fault branching, *Bull. seism. Soc. Am.,* **94,** 202–213.

Brace, W.F. & Byerlee, J.D., 1966. Stick-slip as a mechanism for earthquakes, *Science,* **153**(3739), 990–992.

Brodsky, E.E., Gilchrist, J.J., Sagy, A. & Collettini, C., 2011. Faults smooth gradually as a function of slip, *Earth planet. Sci. Lett.,* **302**(1–2), 185–193.

Caine, J.S., Evans, J.P. & Forster, C.B., 1996. Fault zone architecture and permeability structure, *Geology,* **24**(11), 1025–1028.

Candela, T., Renard, F., Bouchon, M., Schmittbuhl, J. & Brodsky, E.E., 2011a. Stress drop during earthquakes: effect of fault roughness scaling, *Bull. seism. Soc. Am.,* **101**(5), 2369–2387.

Candela, T., Renard, F., Schmittbuhl, J., Bouchon, M. & Brodsky, E.E., 2011b. Fault slip distribution and fault roughness, *Geophys. J. Int.,* **187**(2), 959–968.

Candela, T., Renard, F., Klinger, Y., Mair, K., Schmittbuhl, J. & Brodsky, E.E., 2012. Roughness of fault surfaces over nine decades of length scales, *J. geophys. Res.,* **117,** B08409, doi:10.1029/2011JB009041.

Chester, F.M. & Chester, J.S., 1998. Ultracataclasite structure and friction processes of the Punchbowl fault San Andreas system, California, *Tectonophys.,* **295,** 199–221.

Chester, F.M. & Logan, J.M., 1986. Implications for mechanical properties of brittle faults from observations of the Punchbowl fault zone, California, *Pure appl. Geophys.,* **124**(1), 79–106.

Chester, F.M., Evans, J.P. & Biegel, R.L., 1993. Internal structure and weakening mechanisms of the San Andreas Fault, *J. geophys. Res.,* **98**(B1), 771–786.

Clauset, A., Shalizi, C.R. & Newmann, M.E.J., 2009. Power-law distributions in empirical data, *SIAM Rev.,* **51**(4), 661–703.

Dieterich, J.H. & Kilgore, B.D., 1996. Imaging surface contacts: power law contact distributions and contact stresses in quartz, calcite, glass and acrylic plastic, *Tectonophys.,* **256**(1–4), 219–239.

Dieterich, J.H. & Richards-Dinger, K.B., 2010. Earthquake recurrence in simulated fault systems, in *Seismogenesis and Earthquake Forecasting: The Frank Evison,* Vol. II, pp. 233–250, Springer.

Dieterich, J.H. & Smith, D.E., 2009. Nonplanar faults: mechanics of slip and off-fault damage, *Pure appl. Geophys.,* **166,** 1799–1815.

Dor, O., Ben-Zion, Y., Rockwell, T.K. & Brune, J., 2006. Pulverized rocks in the Mojave section of the San Andreas Fault Zone, *Earth planet. Sci. Lett.,* **245**(3), 642–654.

Dunham, E.M., Belanger, D., Cong, L. & Kozdon, J.E., 2011. Earthquake ruptures with strongly rate-weakening friction and off-fault plasticity. Part 2: nonplanar faults, *Bull. seism. Soc. Am.,* **101**(5), 2308–2322.

Faulkner, D.R., Lewis, A.C. & Rutter, E.H., 2003. On the internal structure and mechanics of large strike-slip fault zones: field observations of the Carboneras fault in southeastern Spain, *Tectonophys.,* **367**(3), 235–251.

Faulkner, D.R., Mitchell, T.M., Rutter, E.H. & Cembrano, J., 2008. On the structure and mechanical properties of large strike-slip faults, *Geol. Soc., Lond., Spec. Publ.,* **299**(1), 139–150.

Faulkner, D.R., Jackson, C.A.L., Lunn, R.J., Schlische, R.W., Shipton, Z.K., Wibberley, C.A.J. & Withjack, M.O., 2010. A review of recent developments concerning the structure, mechanics and fluid flow properties of fault zones, *J. Struct. Geol.,* **32**(11), 1557–1575.

Goebel, T.H.W., Becker, T.W., Schorlemmer, D., Stanchits, S., Sammis, C., Rybacki, E. & Dresen, G., 2012. Identifying fault hetergeneity through mapping spatial anomalies in acoustic emission statistics, *J. geophys. Res.,* **117,** B03310, doi:10.1029/2011JB008763.

Goebel, T.H.W., Schorlemmer, D., Dresen, G., Becker, T.W. & Sammis, C.G., 2013a. Acoustic emissions document stress changes over many seismic cycles in stick-slip experiments, *Geophys. Res. Lett.,* **40,** doi:10.1002/grl.50507.

Goebel, T.H.W., Sammis, C.G., Becker, T.W., Dresen, G. & Schorlemmer, D., 2013b. A comparision of seismicity characteristics and fault structure in stick-slip experiments and nature, *Pure appl. Geophys.,* Top Vol. Multihazard Simulation, doi:10.1007/s00024-013-0713-7.

Goebel, T.H.W., Candela, T., Sammis, C.G., Becker, T.W., Dresen, G. & Schorlemmer, D., 2014. Seismic event distributions and off-fault damage during frictional sliding of saw-cut surfaces with predefined roughness, *Geophys. J. Int.,* **196,** doi:10.1093/gji/ggt401.

Hauksson, E., 2010. Spatial separation of large earthquakes, aftershocks, and background seismicity: analysis of interseismic and coseismic seismicity patterns in southern California, *Pure appl. Geophys.,* **167,** doi:10.1007/s00024-010-0083-3.

Janssen, C., Wagner, F., Zang, A. & Dresen, G., 2001. Fracture process zone in granite: a microstructural analysis, *Int. J. Earth Sci.,* **90**(1), 46–59.

Klinger, Y., 2010. Relation between continental strike-slip earthquake segmentation and thickness of the crust, *J. geophys. Res.,* **115,** B07306, doi:10.1029/2009JB006550.

Mandelbrot, B., 1982. *The Fractal Geometry of Nature,* Freeman.

Mogi, K., 2007. *Experimental Rock Mechanics, Geomechanics Research Series,* Taylor & Francis Group.

Newman, M.E.J., 2005. Power laws, Pareto distributions and Zipf's law, *Contemp. Phys.,* **46**(5), 323–351.

Power, W.L. & Tullis, T.E., 1995. Review of the fractal character of natural fault surfaces with implications for friction and the evolution of fault zones, in *Fractals in the Earth Sciences,* pp. 89–105, eds Barton, C.C. & La Pointe, P.R., Springer.

Powers, P.M. & Jordan, T.H., 2010. Distribution of seismicity across strike-slip faults in California, *J. geophys. Res.,* **115,** doi:10.1029/2008JB006234.

Rockwell, T.K. & Ben-Zion, Y., 2007. High localization of primary slip zones in large earthquakes from paleoseismic trenches: observations and implications for earthquake physics, *J. geophys. Res.,* **112**(B10), B10304, doi:10.1029/2006JB004764.

Rundle, J.B., Rundle, P.B., Donnellan, A. & Fox, G., 2004. Gutenberg-richter statistics in topologically realistic system-level earthquake stress-evolution simulations, *Earth Planets Space,* **56**(8), 761–772.

Sagy, A., Brodsky, E.E. & Axen, G.J., 2007. Evolution of fault-surface roughness with slip, *Geology,* **35,** 283–286.

Savage, H.M. & Brodsky, E.E., 2011. Collateral damage: Evolution with displacement of fracture distribution and secondary fault strands in fault damage zones, *J. geophys. Res.,* **116**(B3), doi:10.1029/2010JB007665.

Schulz, S.E. & Evans, J.P., 2000. Mesoscopic structure of the Punchbowl Fault, Southern California and the geologic and geophysical structure of active strike-slip faults, *J. Struct. Geol.,* **22**(7), 913–930.

Scott, D.R., Lockner, D.A., Beyerlee, J.D. & Sammis, C.G., 1994. Triaxial testing of Lopez fault gouge at 150 MPa mean effective stress, *Pure appl. Geophys.,* **142,** 749–775.

Silverman, B.W., 1986. *Density Estimation for Statistics and Data Analysis,* Chapman and Hall.

Smith, S.A.F., Bistacchi, A., Mitchell, T., Mittempergher, S. & Di Toro, G., 2013. The structure of an exhumed intraplate seismogenic fault in crystalline basement, *Tectonophysics,* **599,** 29–44.

Stanchits, S., Vinciguerra, S. & Dresen, G., 2006. Ultrasonic velocities, acoustic emission characteristics and crack damage of basalt and granite, *Pure appl. Geophys.,* **163,** 975–994.

Tembe, S., Lockner, D.A. & Wong, T.-F., 2010. Effect of clay content and mineralogy on frictional sliding behavior of simulated gouges: binary and ternary mixtures of quartz, illite, and montmorillonite, *J. geophys. Res.,* **115,** B03416, doi:10.1029/2009JB006383.

Turcotte, D.L., 1997. *Fractals and Chaos in Geology and Geophysics,* Cambridge Univ. Press.

Vermilye, J.M. & Scholz, C.H., 1998. The process zone: a microstructural view of fault growth, *J. geophys. Res.,* **103**(B6), 12 223–12 237.

Ward, S.N., 2000. San Francisco bay area earthquake simulations: a step toward a standard physical earthquake model, *Bull. seism. Soc. Am.,* **90**(2), 370–386.

Wechsler, N., Ben-Zion, Y. & Christofferson, S., 2010. Evolving geometrical heterogeneities of fault trace data, *Geophys. J. Int.,* **182**(2), 551–567.

Wesnousky, S.G., 1988. Seismological and structural evolution of strike-slip faults, *Nature,* **335,** 340–342.

Wibberley, C.A.J., Yielding, G. & Di Toro, G., 2008. Recent advances in the understanding of fault zone internal structure: a review, *Geol. Soc., Lond., Spec. Publ.,* **299**(1), 5–33.

Zang, A., Wagner, F.C., Stanchits, S., Janssen, C. & Dresen, G., 2000. Fracture process zone in granite, *J. geophys. Res.,* **105**(B10), 23 651–23 661.

SUPPORTING INFORMATION

Additional Supporting Information may be found in the online version of this article:

Figure S1: Schematic representation of sample geometry and loading conditions for notched Westerly granite samples.
Figure S2: Changes in AE density distributions as function of different sample sizes.
Figure S3: Changes in AE density distributions as function of fault-normal shift of the fault axis.
Figure S4: Changes in AE density distributions as function of variation in rotation angle ($d\mu_f$) used to project the AE events into the corresponding fault coordinate systems.
Figure S5: Changes in fault angle (μ_f) with successive stick-slip events for all four experiments.
Figure S6: Changes in seismic off-fault activity for all experiments. AE densities were computed from all AE events of an experiment, except for events that occurred during the initial ISP which showed the strongest deviations from the average value of γ (http://gji.oxfordjournals.org/lookup/suppl/doi:10.1093/gji/ggu074/-/DC1).

Please note: Oxford University Press is not responsible for the content or functionality of any supporting materials supplied by the authors. Any queries (other than missing material) should be directed to the corresponding author for the article.